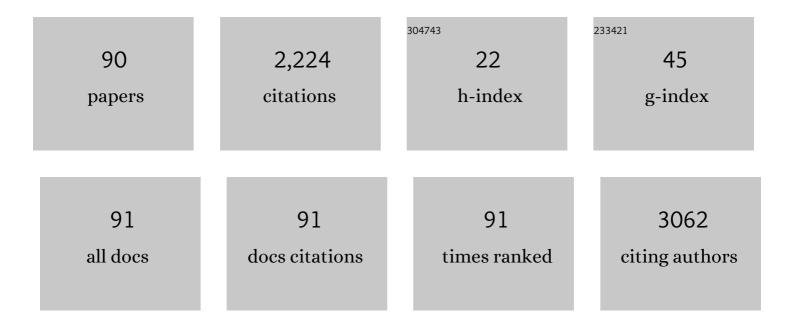
Atsushi K Kono

List of Publications by Year in descending order

Source: https://exaly.com/author-pdf/2856504/publications.pdf Version: 2024-02-01



#	Article	IF	CITATIONS
1	Diversity and determinants of the sigmoid septum and its impact on morphology of the outflow tract as revealed using cardiac computed tomography. Echocardiography, 2022, 39, 248-259.	0.9	4
2	The impact of the atrial wall thickness in normal/mild lateâ€gadolinium enhancement areas on atrial fibrillation patients. Journal of Arrhythmia, 2022, 38, 221-231.	1.2	3
3	Voxel-based analysis of age and gender effects on striatal [1231] FP-CIT binding in healthy Japanese adults. Annals of Nuclear Medicine, 2022, 36, 460-467.	2.2	2
4	Efficacy of myocardial washout of 99mTc-MIBI/Tetrofosmin for the evaluation of inflammation in patients with cardiac sarcoidosis: comparison with 18F-fluorodeoxyglucose positron emission tomography findings. Annals of Nuclear Medicine, 2022, 36, 544-552.	2.2	2
5	Evaluation of aortic calcification using a three-dimensional volume-rendering method in patients with end-stage kidney disease. Journal of Bone and Mineral Metabolism, 2021, 39, 439-445.	2.7	2
6	Feasibility of morphological assessment of coronary artery calcification with electrocardiography-gated non-contrast computed tomography: a comparative study with optical coherence tomography. International Journal of Cardiovascular Imaging, 2021, 37, 1445-1453.	1.5	5
7	Evaluation of microvasculopathy using dualâ \in energy computed tomography in patients with chronic thromboembolic pulmonary hypertension. Pulmonary Circulation, 2021, 11, 1-9.	1.7	10
8	Lateâ€gadolinium enhancement properties associated with atrial fibrillation rotors in patients with persistent atrial fibrillation. Journal of Cardiovascular Electrophysiology, 2021, 32, 1005-1013.	1.7	10
9	Feasibility of catheter ablation in patients with persistent atrial fibrillation guided by fragmented lateâ€gadolinium enhancement areas. Journal of Cardiovascular Electrophysiology, 2021, 32, 1014-1023.	1.7	4
10	Physiological skin FDG uptake: A quantitative and regional distribution assessment using PET/MRI. PLoS ONE, 2021, 16, e0249304.	2.5	1
11	Prevalence and extent of mitral annular disjunction in structurally normal hearts: comprehensive 3D analysis using cardiac computed tomography. European Heart Journal Cardiovascular Imaging, 2021, 22, 614-622.	1.2	55
12	Deep learning model for predicting gestational age after the first trimester using fetal MRI. European Radiology, 2021, 31, 3775-3782.	4.5	22
13	Normative Aortic Valvar Measurements in Adults Using Cardiac Computed Tomography ― A Potential Guide to Further Sophisticate Aortic Valve-Sparing Surgery ―. Circulation Journal, 2021, 85, 1059-1067.	1.6	16
14	Varied Extent of Mitral Annular Disjunction Among Cases With Different Phenotypes of Mitral Valve Prolapse. JACC: Case Reports, 2021, 3, 1251-1257.	0.6	3
15	Prognostic Impact of Myocardial Extracellular Volume Fraction Assessment Using Dualâ€Energy Computed Tomography in Patients Treated With Aortic Valve Replacement for Severe Aortic Stenosis. Journal of the American Heart Association, 2021, 10, e020655.	3.7	19
16	The impact of computed tomography-derived aortic atheroma volume on prognosis after transcatheter aortic valve replacement. International Journal of Cardiology, 2021, 344, 60-65.	1.7	0
17	Does Endovascular Abdominal Aortic Repair Change Psoas Muscle Volume?. Annals of Vascular Surgery, 2020, 63, 162-169.	0.9	2
18	Diagnostic accuracy of deep-learning with anomaly detection for a small amount of imbalanced data: discriminating malignant parotid tumors in MRI. Scientific Reports, 2020, 10, 19388.	3.3	26

#	Article	IF	CITATIONS
19	Simulation Study of Low-Dose Sparse-Sampling CT with Deep Learning-Based Reconstruction: Usefulness for Evaluation of Ovarian Cancer Metastasis. Applied Sciences (Switzerland), 2020, 10, 4446.	2.5	14
20	Revisiting the prevalence and diversity of localized thinning of the left ventricular apex. Journal of Cardiovascular Electrophysiology, 2020, 31, 915-920.	1.7	3
21	Three-dimensional assessment of coronary high-intensity plaques with T1-weighted cardiovascular magnetic resonance imaging to predict periprocedural myocardial injury after elective percutaneous coronary intervention. Journal of Cardiovascular Magnetic Resonance, 2020, 22, 5.	3.3	8
22	Clinical impact of native T1 mapping for detecting myocardial impairment in takotsubo cardiomyopathy. European Heart Journal Cardiovascular Imaging, 2019, 20, 1147-1155.	1.2	22
23	Massive Biventricular Myocardial Calcification in a Patient with Fulminant Myocarditis Requiring Ventricular Assist Device Support. Internal Medicine, 2019, 58, 1283-1286.	0.7	8
24	Filtered back projection revisited in low-kilovolt computed tomography angiography: sharp filter kernel enhances visualization of the artery of Adamkiewicz. Neuroradiology, 2019, 61, 305-311.	2.2	9
25	Focal Myocardial Damage in Cardiac Sarcoidosis Characterized by Strain Analysis on Magnetic Resonance Tagged Imaging in Comparison with Fluorodeoxyglucose Positron Emission Tomography Accumulation and Magnetic Resonance Late Gadolinium Enhancement. Journal of Computer Assisted Tomography. 2018. 42. 607-613.	0.9	3
26	Japanese multicenter database of healthy controls for [1231]FP-CIT SPECT. European Journal of Nuclear Medicine and Molecular Imaging, 2018, 45, 1405-1416.	6.4	80
27	Effects of Lanthanum Carbonate on Coronary Artery Calcification and Cardiac Abnormalities After Initiating Hemodialysis. Calcified Tissue International, 2018, 102, 310-320.	3.1	22
28	Dominant Spinal Feeder Through Arterial "Basket―of Conus Medullaris. Annals of Thoracic Surgery, 2018, 106, e207.	1.3	0
29	Integrating CT Myocardial Perfusion andÂCT-FFR in the Work-Up ofÂCoronaryÂArteryÂDisease. JACC: Cardiovascular Imaging, 2017, 10, 760-770.	5.3	130
30	The differences between bisecting and offâ€center cuts of the aortic root: The threeâ€dimensional anatomy of the aortic root reconstructed from the living heart. Echocardiography, 2017, 34, 453-461.	0.9	21
31	The association between wedging of the aorta and cardiac structural anatomy as revealed using multidetectorâ€row computed tomography. Journal of Anatomy, 2017, 231, 110-120.	1.5	17
32	Tailored Duration of Contrast Material Injection in High-Pitch Computed Tomographic Aortography With a Double-Level Test Bolus Method. Investigative Radiology, 2017, 52, 274-280.	6.2	5
33	Relationship between cardiac calcification and left ventricular hypertrophy in patients with chronic kidney disease at hemodialysis initiation. Heart and Vessels, 2017, 32, 1109-1116.	1.2	26
34	Spontaneous coronary artery intramural hematoma in a patient with vascular Ehlers-Danlos syndrome: Serial findings in coronary computed tomographic angiography. Journal of Cardiovascular Computed Tomography, 2017, 11, 324-326.	1.3	1
35	<pre><scp>D</scp>iversity and <scp>D</scp>eterminants of the <scp>T</scp>hreeâ€dimensional <scp>A</scp>natomical <scp>A</scp>xis of the <scp>H</scp>eart as <scp>R</scp>evealed <scp>U</scp>sing <scp>M</scp>ultidetectorâ€row <scp>C</scp>omputed <scp>T</scp>omography. Anatomical Record, 2017, 300, 1083-1092.</pre>	1.4	9
36	Anatomical Record, 2017, 300, 1083-1092. Advantages of 70-kV CT Angiography for the Visualization of the Adamkiewicz Artery: Comparison with 120-kV Imaging. American Journal of Neuroradiology, 2017, 38, 2399-2405.	2.4	15

#	Article	IF	CITATIONS
37	Application of dual-energy CT to suppression of metal artefact caused by pedicle screw fixation in radiotherapy: a feasibility study using original phantom. Physics in Medicine and Biology, 2017, 62, 6226-6245.	3.0	5
38	Diagnostic value of transmural perfusion ratio derived from dynamic CT-based myocardial perfusion imaging for the detection of haemodynamically relevant coronary artery stenosis. European Radiology, 2017, 27, 2309-2316.	4.5	33
39	Heart failure diagnosis for tagged magnetic resonance images. , 2017, , .		2
40	An Isolated Case of Late-onset Amyloidogenic Transthyretin Type Familial Amyloid Polyneuropathy Associated with a Mutant Transthyretin Substituting Methionine for Valine at Position 30 Showing Latent Progressive Cardiac Involvement Confirmed by Serial Annual Electrocardiograms. Internal Medicine, 2017, 56, 163-168.	0.7	2
41	Pulmonary artery domain region extraction from MDCT image. International Journal of Applied Electromagnetics and Mechanics, 2016, 52, 479-486.	0.6	0
42	Slitâ€Like Deformation of the Coronary Sinus Orifice due to Compression of the Inferior Pyramidal Space by the Severely Dilated Left Ventricle. PACE - Pacing and Clinical Electrophysiology, 2016, 39, 1026-1029.	1.2	4
43	Compression of the Right Ventricular Outflow Tract due to Straight Back Syndrome Clarified by Low-dose Dual-source Computed Tomography. Internal Medicine, 2016, 55, 3279-3283.	0.7	7
44	Characteristics of Residual Atrial Posterior Wall and Roofâ€Dependent Atrial Tachycardias after Pulmonary Vein Isolation. PACE - Pacing and Clinical Electrophysiology, 2016, 39, 1090-1098.	1.2	3
45	Clinical cardiac structural anatomy reconstructed within the cardiac contour using multidetectorâ€row computed tomography: Atrial septum and ventricular septum. Clinical Anatomy, 2016, 29, 342-352.	2.7	16
46	Clinical cardiac structural anatomy reconstructed within the cardiac contour using multidetectorâ€row computed tomography: Left ventricular outflow tract. Clinical Anatomy, 2016, 29, 353-363.	2.7	15
47	Clinical cardiac structural anatomy reconstructed within the cardiac contour using multidetectorâ€row computed tomography: The arrangement and location of the cardiac valves. Clinical Anatomy, 2016, 29, 364-370.	2.7	9
48	Coronary CT angiography derived fractional flow reserve: Methodology and evaluation of a point of care algorithm. Journal of Cardiovascular Computed Tomography, 2016, 10, 105-113.	1.3	50
49	Serum phosphate is an independent predictor of the total aortic calcification volume in non-hemodialysis patients undergoing cardiovascular surgery. Journal of Cardiology, 2016, 68, 308-315.	1.9	2
50	Four-dimensional noise reduction using the time series of medical computed tomography datasets with short interval times: a static-phantom study. PeerJ, 2016, 4, e1680.	2.0	5
51	A Comparison of Quantitative T2 Mapping on Cardiovascular Magnetic Resonance Imaging with Metaiodobenzylguanidine Scintigraphy and Left Ventricular Functional Recovery in Dilated Cardiomyopathy: A Retrospective Pilot Study. Internal Medicine, 2015, 54, 2121-2128.	0.7	3
52	Use of Coils and a Pulmonary Vasodilator to Reduce Pulmonary Hypertension in a Patient with Interstitial Pneumonia and Scleroderma. Internal Medicine, 2015, 54, 2721-2726.	0.7	0
53	Clinical structural anatomy of the inferior pyramidal space reconstructed from the living heart: Threeâ€dimensional visualization using multidetectorâ€row computed tomography. Clinical Anatomy, 2015, 28, 878-887.	2.7	20
54	Optimal angulations for obtaining an en face view of each coronary aortic sinus and the interventricular septum: Correlative anatomy around the left ventricular outflow tract. Clinical Anatomy, 2015, 28, 494-505.	2.7	16

#	Article	IF	CITATIONS
55	Dynamic Blood Oxygen Level-dependent MR Imaging of Muscle: Comparison of Postocclusive Reactive Hyperemia in Young Smokers and Nonsmokers. Magnetic Resonance in Medical Sciences, 2015, 14, 275-283.	2.0	8
56	Tumor segmentation on FDG-PET: usefulness of locally connected conditional random fields. , 2015, , .		1
57	Quantification of the myocardial area at risk using coronary CT angiography and Voronoi algorithm-based myocardial segmentation. European Radiology, 2015, 25, 49-57.	4.5	56
58	Bone marrow magnetic resonance imaging of the clivus in pediatric leukemia patients and normal controls. Japanese Journal of Radiology, 2015, 33, 146-152.	2.4	6
59	Three-dimensional quantification and visualization of aortic calcification by multidetector-row computed tomography: A simple approach using a volume-rendering method. Atherosclerosis, 2015, 239, 622-628.	0.8	19
60	Fractional Flow Reserve Computed from Noninvasive CT Angiography Data: Diagnostic Performance of an On-Site Clinician-operated Computational Fluid Dynamics Algorithm. Radiology, 2015, 274, 674-683.	7.3	218
61	Reconstruction of an Extracardiac Aortocoronary Collateral and Simulation of Selective Angiography With Multidetector-Row Computed Tomography. Circulation, 2015, 131, e476-9.	1.6	2
62	Clinical Structural Anatomy of the Inferior Pyramidal Space Reconstructed Within the Cardiac Contour Using Multidetectorâ€Row Computed Tomography. Journal of Cardiovascular Electrophysiology, 2015, 26, 705-712.	1.7	22
63	Evaluation of blood volume by use of blood oxygen level-dependent magnetic resonance imaging in a cuff-compression model: usefulness of calculated echo time image. Japanese Journal of Radiology, 2015, 33, 441-447.	2.4	1
64	Cardiovascular magnetic resonance tagging imaging correlates with myocardial dysfunction and T2 mapping in idiopathic dilated cardiomyopathy. International Journal of Cardiovascular Imaging, 2014, 30, 145-152.	1.5	11
65	Association between the rotation and threeâ€dimensional tortuosity of the proximal ascending aorta. Clinical Anatomy, 2014, 27, 1200-1211.	2.7	14
66	Relative Myocardial Blood Flow by Dynamic Computed Tomographic Perfusion Imaging Predicts Hemodynamic Significance of Coronary Stenosis Better Than Absolute Blood Flow. Investigative Radiology, 2014, 49, 801-807.	6.2	59
67	Cardiovascular magnetic resonance T2 mapping can detect myocardial edema in idiopathic dilated cardiomyopathy. International Journal of Cardiovascular Imaging, 2014, 30, 65-72.	1.5	35
68	Corrigendum to "Respiratory-gated 18F-FDG PET/CT for the diagnosis of liver metastasis―[Eur. J. Radiol. 82 (10) (2013) 1696–1701]. European Journal of Radiology, 2014, 83, 741.	2.6	0
69	The feasibility of a 64-slice MDCT for detection of the Adamkiewicz artery: comparison of the detection rate of intravenous injection CT angiography using a 64-slice MDCT versus intra-arterial and intravenous injection CT angiography using a 16-slice MDCT. International Journal of Cardiovascular Imaging, 2013, 29, 127-133.	1.5	10
70	Respiratory-gated 18F-FDG PET/CT for the diagnosis of liver metastasis. European Journal of Radiology, 2013, 82, 1696-1701.	2.6	14
71	18F-FDG-PET/CT findings of retroperitoneal tumors: a pictorial essay. Japanese Journal of Radiology, 2013, 31, 301-309.	2.4	13
72	Prevalence of Dural Ectasia in Loeys-Dietz Syndrome: Comparison with Marfan Syndrome and Normal Controls. PLoS ONE, 2013, 8, e75264.	2.5	20

#	Article	IF	CITATIONS
73	Potential contribution of multiplanar reconstruction (MPR) to computer-aided detection of lung nodules on MDCT. European Journal of Radiology, 2012, 81, 366-370.	2.6	11
74	3D automatic exposure control for 64-detector row CT: Radiation dose reduction in chest phantom study. European Journal of Radiology, 2011, 77, 522-527.	2.6	18
75	Dynamic late gadolinium enhancement simply quantified using myocardium to lumen signal ratio: Normal range of ratio and diffuse abnormal enhancement of cardiac amyloidosis. Journal of Magnetic Resonance Imaging, 2011, 34, 50-55.	3.4	15
76	High prevalence of vertebral artery tortuosity of Loeys-Dietz syndrome in comparison with Marfan syndrome. Japanese Journal of Radiology, 2010, 28, 273-277.	2.4	24
77	Late gadolinium enhancement on cardiac magnetic resonance imaging: is it associated with a higher incidence of nonsustained ventricular tachycardia in patients with idiopathic dilated cardiomyopathy?. Japanese Journal of Radiology, 2010, 28, 355-361.	2.4	10
78	Utility of phase contrast MR imaging for assessment of pulmonary flow and pressure estimation in patients with pulmonary hypertension: Comparison with right heart catheterization and echocardiography. Journal of Magnetic Resonance Imaging, 2009, 30, 973-980.	3.4	58
79	Dual-energy CT head bone and hard plaque removal for quantification of calcified carotid stenosis: utility and comparison with digital subtraction angiography. European Radiology, 2009, 19, 2060-2065.	4.5	100
80	Comparison of grey matter and metabolic reductions in frontotemporal dementia using FDG-PET and voxel-based morphometric MR studies. European Journal of Nuclear Medicine and Molecular Imaging, 2008, 35, 2227-2234.	6.4	100
81	Quantitative and qualitative assessment of non-contrast-enhanced pulmonary MR imaging for management of pulmonary nodules in 161 subjects. European Radiology, 2008, 18, 2120-2131.	4.5	88
82	Comparison of Regional Brain Volume and Glucose Metabolism Between Patients with Mild Dementia with Lewy Bodies and Those with Mild Alzheimer's Disease. Journal of Nuclear Medicine, 2007, 48, 704-711.	5.0	81
83	Cerebral perfusion pattern of idiopathic normal pressure hydrocephalus studied by SPECT and statistical brain mapping. Annals of Nuclear Medicine, 2007, 21, 39-45.	2.2	54
84	Fully automatic differential diagnosis system for dementia with Lewy bodies and Alzheimer's disease using FDG-PET and 3D-SSP. European Journal of Nuclear Medicine and Molecular Imaging, 2007, 34, 1490-1497.	6.4	51
85	Fully automatic diagnostic system for early- and late-onset mild Alzheimer's disease using FDG PET and 3D-SSP. European Journal of Nuclear Medicine and Molecular Imaging, 2006, 33, 575-583.	6.4	68
86	Early disappearance of calcification in posterior paraspinal muscles in a patient with rhabdomyolysis associated with neuroleptic malignant syndrome. Radiation Medicine, 2006, 24, 463-466.	0.8	0
87	Automatic volumetric measurement of segmented brain structures on magnetic resonance imaging. Radiation Medicine, 2006, 24, 422-430.	0.8	21
88	Usefulness of intravascular ultrasonography for treatment of a ruptured vertebral dissecting aneurysm. Radiation Medicine, 2006, 24, 577-582.	0.8	4
89	Comparison of gray matter and metabolic reduction in mild Alzheimer's disease using FDG-PET and voxel-based morphometric MR studies. European Journal of Nuclear Medicine and Molecular Imaging, 2005, 32, 959-963.	6.4	81
90	Voxel-based morphometric comparison between early- and late-onset mild Alzheimer's disease and assessment of diagnostic performance of z score images. American Journal of Neuroradiology, 2005, 26, 333-40.	2.4	156